Methamphetamine-induced apoptosis in glial cells examined under marker-free imaging modalities

Lianna Y. D'Brant
Habben Desta
Ting Chean Khoo
Anna V. Sharikova
Supriya D. Mahajan
Alexander Khmaladze

SPIE.

Methamphetamine-induced apoptosis in glial cells examined under marker-free imaging modalities

Lianna Y. D'Brant,[a] Habben Desta,[a] Ting Chean Khoo,[a] Anna V. Sharikova,[b] Supriya D. Mahajan,[a] and Alexander Khmaladze[a,*]

[a]State University of New York System (SUNY), Albany, New York, United States
[b]State University of New York, Jacobs School of Medicine & Biomedical Sciences, Buffalo, New York, United States

Abstract. We used phase microscopy and Raman spectroscopic measurements to assess the response of *in vitro* rat C6 glial cells following methamphetamine treatment in real time. Digital holographic microscopy (DHM) and three-dimensional (3-D) tomographic nanoscopy allow measurements of live cell cultures, which yield information about cell volume changes. Tomographic phase imaging provides 3-D information about the refractive index distribution associated with the morphology of biological samples. DHM provides similar information, but for a larger population of cells. Morphological changes in cells are associated with alterations in cell cycle and initiation of cell death mechanisms. Raman spectroscopy measurements provide information about chemical changes within the cells. Our Raman data indicate that the chemical changes in proteins preceded morphological changes, which were seen with DHM. Our study also emphasizes that tomographic phase imaging, DHM, and Raman spectroscopy are imaging tools that can be utilized for noninvasive simultaneous monitoring of morphological and chemical changes in cells during apoptosis and can also be used to monitor other dynamic cell processes. © *The Authors. Published by SPIE under a Creative Commons Attribution 4.0 Unported License. Distribution or reproduction of this work in whole or in part requires full attribution of the original publication, including its DOI.* [DOI: 10.1117/1.JBO.24.4.046503]

1 Introduction

Methamphetamine hydrochloride (METH) is the second most widely abused illicit drug in the world. METH increases the release of dopamine, which induces neurotoxic responses in the human brain. These neurotoxic responses can lead to neural damage and cellular apoptosis.[1,2] METH abuse results in neurotoxic damage to dopaminergic nerve terminals and leads to cellular degeneration and cell death.[3,4] Since METH is a cationic lipophilic molecule, it can diffuse through the cellular membrane to the mitochondria, resulting in the perturbation of normal mitochondrial function and the induction of mitochondrial toxicity.[4,5] This creates a buildup of positively charged molecules within the mitochondria, interfering with the electrochemical gradient established by the electron transport chain. This electrochemical gradient is necessary for adenosine triphosphate (ATP) synthesis and mitochondrial membranes.[6] These functions are essential for cell survival, and failure in these functions initiates signaling cascade, which results in cell death. To assess mitochondrial dysfunction in cells, investigators quantify the cells' ability to produce ATP in response to energy demands.[7] The underlying mechanisms by which METH infiltrates the neural pathways remain enigmatic.

Recent studies have shown that acute and chronic METH use leads to neurotoxicity in the brain, which further deteriorates into neural damage, including morphological abnormalities.[8–10] Since glia cells are the resident macrophages, they respond to central nervous system (CNS) injury. Studies have shown that macrophage population significantly decreases after METH exposure.[11,12] We hypothesize that METH affects mitochondria-dependent pathways resulting in neuronal apoptosis.

Apoptosis is, morphologically and biochemically, a form of cell death, often in response to physiological and pathological circumstances.[13,14] Response to drug stimuli can cause neuronal apoptosis, leading to neurocognitive disorders that may progress to neurological diseases like dementia and Alzheimer's disease.[15] METH treatment causes DNA fragmentation and dysfunction in the nigrostriatum in the brain.[13,16–18] The striatum is a basal ganglia nucleus that controls the motor execution and motor inhibition,[19] and regulates reward-oriented behavior.[20] The basal ganglia receive excitatory signals from the prefrontal cortex. Imbalance in these brain regions can cause severe irreversible alterations. This can lead to a cascade of effects that ultimately cause CNS cytotoxicity and neuronal dysfunction. Cell volume loss is a morphological hallmark of cell death, and apoptotic cell volume decrease is associated with programmed cell death.[21–23] To quantify cell volume changes, we used two label-free imaging approaches, Nanolive three-dimensional (3-D) Cell Explorer and DHM, measuring cell volume post-METH treatment on C6 rat glia cultures. We also attempted to describe the effect of METH-induced apoptosis in C6 glial cells.

The light absorption of cells is too low to generate sufficient amplitude changes in the transmitted light. This makes it difficult to visualize cells and their structure under a light microscope without a system to enhance optical contrast. One solution to this is to introduce dyes as markers, isolating specific molecules, such as proteins. There are various techniques to label cells, such as immunolabeling using antibodies[24,25] and intracellular injections of fluorescent molecules.[26] Immunolabeled samples need to be fixed first, typically with paraformaldehyde, which preserves the cells, but they are no longer metabolically active. In addition, immunolabeling can lead to phototoxicity of the cells or photobleaching under the illumination of a microscope.[27,28] Phototoxicity is the generation of reactive oxygen species (ROS)

that may have adverse effects on the cell physiology, resulting in cell impairment.[29] It is challenging to directly visualize the intracellular events leading to apoptosis in real time.[30] To avoid the limitations associated with cell fixation and traditional immunolabeling techniques, we can use the refractive index (RI) of cells to enhance an image contrast.[28]

The 3-D tomographic imaging employs a label-free technique for investigating biological samples on the nanometer scale.[31,32] The microscope can visualize 3-D structures by detecting spatial changes in RI, thus rendering staining unnecessary in various biological samples.[33] After a series of holograms is collected by the hardware, high-resolution images of each plane are created by computer processing, and quantitative digital staining is performed. The digital stain is based on two parameters: the RI and the index gradient (IG) (e.g., low RI and high gradient are typical for membrane structures). This technique provides 3-D cell imaging in real time, allowing monitoring of morphological changes during apoptosis.

Digital holographic microscopy (DHM) is a phase-contrast imaging technique, which measures the effects of a sample on the laser light passing through it. Similar to the Zernike phase contrast microscopy, DHM can be used to visualize phase objects. These objects appear transparent, but they produce a distinguishable shift in the phase of a coherent light source.[34] DHM can be used to measure changes in cellular volume associated with cellular apoptosis, such as absolute cell volume and cell death, in real time,[35–37] making this technique suitable for sensitive measurement of cellular events.[38] DHM is based on interferometry. It can, therefore, detect optical path length variation with nanometer accuracy. This is often employed to investigate the thickness and the RI of cells.[39,40]

A standard DHM setup consists of a coherent illumination source that propagates through (or is reflected from) the sample, producing an interference pattern captured by a CCD camera. From the interference pattern, the sample image can be reconstructed using an appropriate computer algorithm. The illumination source is typically a laser, such as He–Ne, diode, argon, or sapphire femtosecond lasers.[41,42] DHM provides direct access to the quantitative phase, which can be used to map the changes in the optical path length.[43] From the known index of refraction, the optical path length is then converted to the physical thickness of the sample, providing the height of the sample:

$$h(x, y) = \frac{\lambda}{2\pi} \frac{\phi(x, y)}{n - n_0},\qquad(1)$$

where λ is the wavelength of the laser, n is the RI of the sample, n_0 is the RI of the surrounding media, and ϕ is the phase map obtained from the holographic reconstruction of the wavefront.

DHM is an efficient, easy-to-operate, noninvasive phase-contrast microscopy technique capable of imaging transparent samples, such as living cell cultures. DHM provides the quantitative spatial distribution of the optical path lengths created by transparent specimens. This quantitative distribution contains information concerning both morphology and RI of the observed sample. In addition, the high sensitivity of these phase-shift measurements allows one to achieve subwavelength axial accuracy.[44] Since the creation and capture of an interference pattern requires the light of low intensity, the sample is free from photodamage. Thus, DHM is a label-free imaging technique capable of distinguishing cellular morphological changes.[38]

In order to investigate the structural changes in cell tissues, which accompany the morphological changes monitored by DHM, we applied Raman spectroscopy, a technique commonly used to provide a spectral fingerprint by which molecules can be identified. This technique relies on inelastic, or Raman, scattering, first discovered by Raman and Krishnan in 1928.[45] Raman scattering is generated by a laser, typically a diode-pumped single-longitudinal mode laser, directed onto the cell. The difference in energy between the incident and scattered photons corresponds to the energy required to excite a particular molecular vibration. Detection of these scattered photons produces a Raman spectrum, consisting of different bands that correspond to the vibrational frequencies of different functional groups.[46,47] Raman spectroscopy is a routine application in the field of biochemistry, providing information about cells and tissues; it can also be a diagnostic tool in clinical studies.[48,49] For example, Raman spectra can differentiate between viable and nonviable tissue constructs.[50,51] Raman spectroscopy can also be used to image bone tissue.[52–54]

Raman spectrometry can detect changes in cellular cultures and is commonly implemented to study the growth, death, chemical changes, etc., within cell cultures in real time. Spectral changes provide information about cell cycle progression, as they represent changes in protein, nucleic acid, and lipids content.[55]

In this study, we evaluated cellular apoptosis in live CNS rat glia cells (C6) using noninvasive, marker-free imaging techniques. We employed two-phase imaging modalities to measure apoptotic volume decrease (APD)in cells. In addition, we digitally stained for mitochondria and quantified the mitochondria volume loss. Raman spectroscopy was used to monitor the chemical changes during apoptosis.

2 Experimental Methods

2.1 Administered Substances

Doxorubicin hydrochloride (DOX), a chemotherapy drug known to induce apoptosis, was obtained from Sigma (Cat. No. 44583). DOX targets rapidly dividing cells and inserts between adjunct nucleotides, disrupting DNA synthesis and transcription, and triggering an apoptotic cascade. DOX was used as a positive control in all our experiments. It was administered at a concentration of 1 μM in the cellular growth medium. All cytotoxic evaluation studies using doxorubicin range between 1 and 2 μM.[56,57]

METH was obtained from Sigma (Cat. No. M8750, St. Louis, Massahusetts) and dissolved in RNase/DNase-free water at a concentration of 10 mg/ml and used in our cell culture experiments at a concentration of 100 μM. It has been demonstrated that a single METH injection rapidly and reversibly decreases the activity of the dopamine transporter.[58,59] Thus, to investigate the acute effects of methamphetamine on C6 glia cells, we used a range of methamphetamine concentration from 10 to 100 μM, similar to what were used previously.[58] Typically, *in vitro* studies that evaluate acute METH effects or single-dose administration use methamphetamine concentration ranging from 10 to 100 μM. When glia were treated with 10 μM dose of METH, we did not observe any significant changes in mitochondrial respiration and glycolytic activity, however, when glia were treated with a 100 μM dose of METH, we observed consistent and significant changes in apoptotic genes and protein expression, as well as greater mitochondrial respiration and glycolytic activity, indicating convergence of oxidative stress, neuroinflammatory

responses, and mitochondrial dysfunction at that dose of METH. We, therefore, used the 100 μM METH dose for all other experiments in our study.[22]

2.2 C6 Glial Cell Cultures

Cultured rat C6 glial cells were purchased from ATCC (Cat# ATCC CCL-107). About 60,000 cells/ml were seeded onto a 35-mm glass bottom imaging dish provided by Idibi (Cat# 81218-200) in Dulbecco's modified Eagle medium (DMEM) nutrient mixture F-12 media from Thermo Fisher (Cat# DMEM/F-12) supplemented with 10% fetal bovine serum (FBS), and were treated with with DOX (1 μM) or METH (100 μM). Cell volume was measured using Nanolive 3-D Cell Explorer and DHM system.

2.3 Nanolive 3-D Cell Explorer Measurements

We transferred C6 glial cells from the incubator to the top-stage incubator of the Nanolive 3-D Cell Explorer when they were ready to be imaged. Cells were grown to ~70% confluence, to have enough cells within the field-of-view and still be able to image individual cells. The cells were maintained at 37°C, 5% CO_2 to 95% O_2 and 95% humidity during image acquisition. We acquired z-stack images on Nanolive 3-D Cell Explorer (Nanolive, San Francisco) with a 60× air objective (numerical aperture = 0.8). Z-stack images were stored at a resolution of $512 \times 512 \times 96$ (94 μm × 94 μm × 0.36 μm). We could typically image 10 to 15 individual cells within the field-of-view of the microscope.

The stage included a thermal controller, a carbogen mixer, a humidity module, and a chamber for the 35-mm glass-bottom dish. The stage produced and maintained a vertical temperature gradient to reduce condensation on the glass cover of the environmental chamber and kept the cells in a controlled environment while imaging live cells.

Nanolive 3-D Cell Explorer generated a series of holograms at different angles, which were then used to create a 3-D cell image. The raw data displayed the spatial distribution of the RI as a 96-image z-stack in grayscale at 2 frames per second (fps).[31]

The digital staining was done by selecting the range of values of RI and refractive IG, which were then displayed as a 3-D map. Parameters were chosen to isolate a specific part of the cell, corresponding to specific cell bodies, such as cytoplasm. The microscope collected a vertical stack of images (z-stack), which was used to evaluate the volume of the cell. In the z-stack, we measured the number of pixels for each digitally stained channel using an image processing software (Fiji—https://fiji.sc/). The stack files were segmented using the segmentation editor and reconstructed as a series of 40 stacks, in preparation for volume analysis. To evaluate the cell volume, acquired data were exported as image stack files and analyzed using Fiji. Volume data were computed by counting the number of all digitally stained pixels within a region of interest. Three different regions at each time point were analyzed.

2.4 Digital Holographic Microscopy

Figure 1 shows our DHM setup. The beam from a He–Ne laser (633 nm) traveled through a microscope objective and a plano-convex lens L_1. As the laser beam exited the plano-convex lens, it was collimated and had a large cross-sectional area. Lens L_2
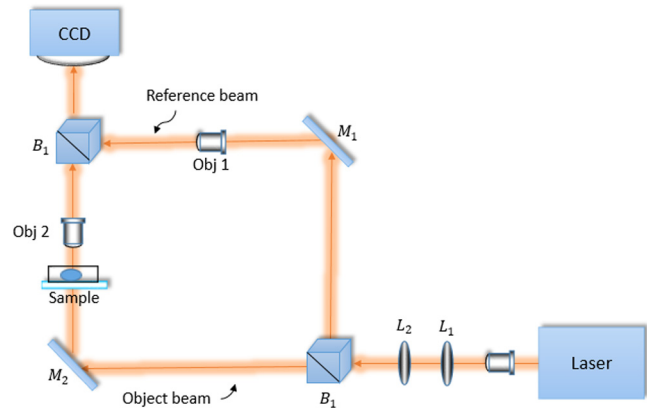

Fig. 1 Transmission DHM setup. The 633-nm laser beam travels through a microscope objective and lens L_1 generating a collimated beam. Lens L_1 focuses the beam on the back focal plane of the microscope objectives OBJ_1 and OBJ_2. Beamsplitter B_1 splits the beam into the reference and object arms. The reference beam travels to a plane mirror M_1, where it is reflected to OBJ_1 and into B_2, recombining with the object beam. The object beam travels to M_2, where it is directed through the cell culture sample maintained in an environmental chamber (ibidi Nanolive heating system/temperature controller/gas incubation system), mounted on a 3-D translation stage.

focused the beam on the back focal plane of the microscope objectives OBJ_1 and OBJ_2. The beamsplitter B_1 separated the beam into the reference and object arms. The reference beam traveled to a plane mirror M_1, where it was reflected to the microscope objective OBJ_1 and into second beamsplitter B_2, recombining with the object beam. Plane mirror M_2 directed the object beam through the cell culture sample maintained in an environmental chamber (ibidi Nanolive heating system/temperature controller/gas incubation system), mounted on a 3-D translation stage. OBJ_2 was used to form an image on the CCD camera.

We calculated the total cell volume by summing the values of all pixels within the field-of-view, after the background subtraction and adjustment for the RI using Eq. (1). We were able to image ~450 individual cells within the field-of-view of the microscope.

Cell cultures were taken from the incubator, the media was changed, and the cells were placed in the environmental chamber with regulated 5% CO_2 to 95% O_2 (carbogen) gas, the temperature of 37°C, and 95% humidity for 3 h. The first set of experiments was done to evaluate the apoptotic effects of doxorubicin (DOX), which served as a control. C6 cells were treated with a dose of DOX (1 μM), and the cell volume was measured using DHM in 10-min intervals. Similarly, the second set of experiments was done to evaluate the apoptotic effect of METH on C6 glial cells, which were treated with 100-μM METH.

2.5 Raman Spectroscopy

Raman spectra were acquired by a commercial microspectroscope (HORIBA XploRA PLUS). This Raman spectrometer was equipped with a 1024×256 TE air cooled CCD chip (pixel size: 26 μm, temperature: −60°C). HORIBA's LabSpec6 software was used for data acquisition, fluorescent background removal, baseline correction, and peak fitting. The excitation wavelength was 785 nm. Entrance slit of 50 μm produced an approximate spectral resolution of 4 cm^{-1}.

Cells were grown on a quartz substrate to minimize the effects of fluorescence. Each substrate with cells was kept in the incubator until it was used for measurements. The measurements were done at several time points after the cell treatment. For each of the time points, three measurements of three accumulations of 60 s each were acquired.

3 Results

We evaluated the apoptotic effects of DOX, which served as a control. C6 cells were treated with a dose of DOX (1 μM), and the cell volume was measured using Nanolive 3-D Cell Explorer in 10-min intervals [Fig. 2(a)]. We digitally stained the cells (in red). Parameters of RI and IG were kept consistent when staining (mean $\pm$ SEM; RI: 1.3400 ± 0.0003, IG: 0.01000 ± 0.0005). When cells were treated with DOX, a significant decrease in cell volume was observed within 30 min [Fig. 2(b)]. Cell volume continued to decrease with time. After 120 min, the cells began to detach from the glass substrates, which made further volume measurements unreliable. By that time, the cell volume decreased to 40% of the original volume. We studied the effects of DOX treatment in the mitochondria and found that the mitochondrial volume decreased significantly [$t = 0$ min: 100%, $t = 120$ min: $10.92 \pm 6.52\%$, $**p = 0.005$; Fig. 3(a)]. We digitally stained for the mitochondria, setting the parameters for RI and IG [RI: 1.3400 ± 0.0004, IG: 0.016 ± 0.004; Fig. 3(b)].

The second experiment was done to evaluate the apoptotic effect of METH on C6 glial cells [Fig. 4(a)]. The cells were treated with 100-μM METH. A substantial decrease in cell volume was observed within 50 min after METH treatment. By that time, the cell volume fell below 70% of the original volume [Fig. 4(b)]. In addition, we studied the effects of METH treatment in the mitochondria, where we observed a significant decrease in volume [$t = 0$: 100%, $t = 120$: $9 \pm 9\%$, $*p = 0.038$; Fig. 5(a)]. The digital staining was applied to the mitochondria

shown on the first panel, and these parameters were kept for the remaining images for the duration of the experiment [RI: 1.33000 ± 0.00005; IG: 0.00300 ± 0.00008; Fig. 5(b)]. Similar to what we found in DOX-treated cells, the overall mitochondria volume decreased significantly post-METH treatment.

Our DHM experiments were done on the cultured cells ($\sim$5000 cells) that were placed in an environmental chamber. Figure 6 shows the percent volume changes in C6 cells as a result of APD. In the case of DOX-induced apoptosis, a substantial decrease in cell volume was observed within 40 min after DOX treatment. Cellular volume continued to decrease with time. After 150 min, the cells were detaching from the glass bottom dish they were kept in, which made further volume measurements unreliable. By that time, the cell volumes decreased to 40% of the original volume. For METH-induced apoptosis, after 200 min, cell culture volume decreased to 60% of its original value. (The difference between Nanolive cytoplasm volume measurements and DHM measurements are likely due to the difference in the number of cells that were imaged.)

Figure 7 shows typical Raman spectra obtained from the cell cultures at various stages of apoptosis. For these measurements, two sets of four Petri dishes with cells were treated simultaneously either with 1-μM DOX or 100-μM METH. Later, each dish was removed from the incubator and placed on the sample stage of Raman microspectroscope, so that C6 spectra were collected at several time points ($t = 0$ min, $t = 50$ min, $t = 100$ min, and $t = 150$ min after the induction of apoptosis). For comparison, untreated control cell cultures spectra taken 200 min apart were also acquired.

The spectra were background subtracted, and the peaks at 1003, 1092, 1155, 1340, 1447, and 1655 cm^{-1}, which are indicative of molecular vibrations in lipids, nucleic acid, and proteins,[60] were fitted. Since in our previous work,[61] the intensity of phenylalanine peak at 1003 cm^{-1} remained approximately the
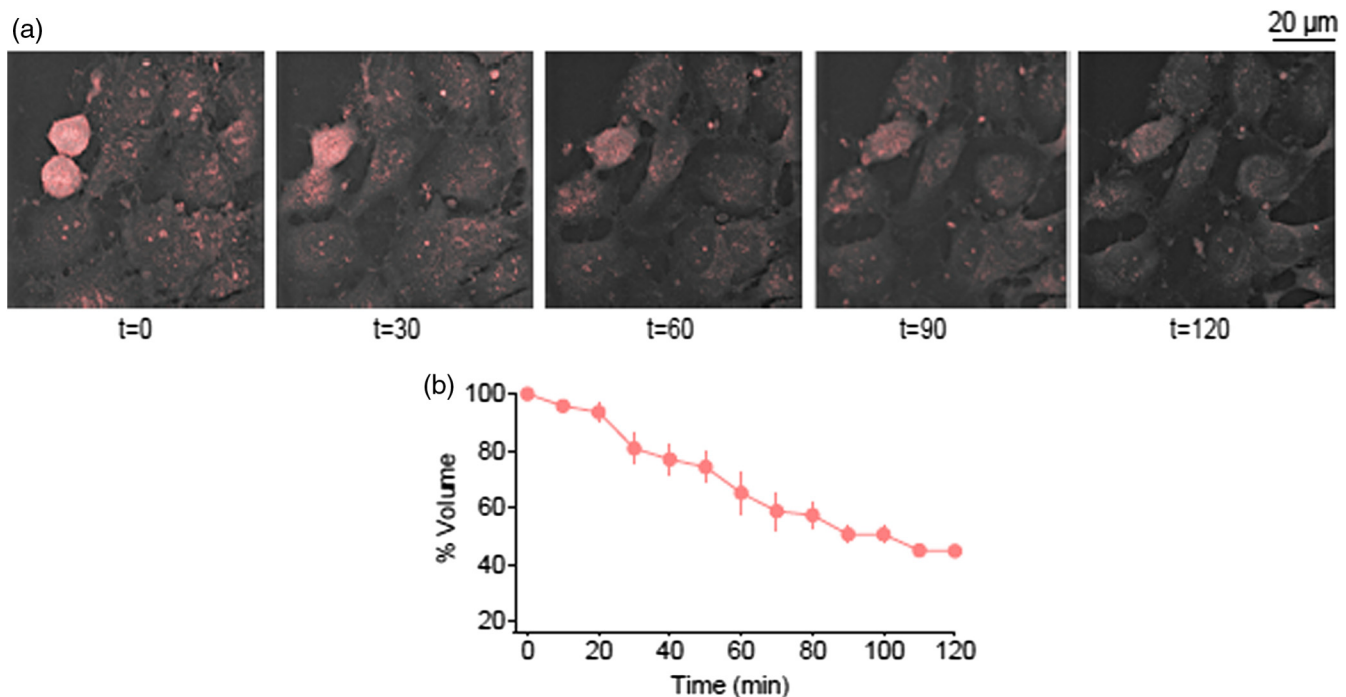

Fig. 2 Cell volume data of C6 glia cells treated with DOX. (a) Images of cells after digital staining, starting at $t = 0$ min in 30-min intervals. (b) Apoptotic volume changes.
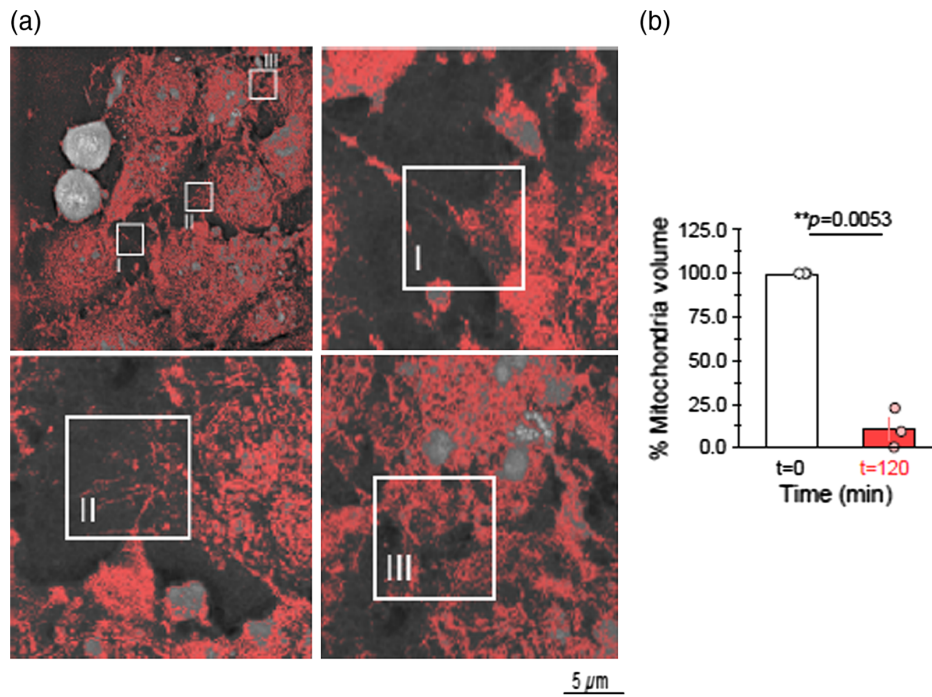
Fig. 3 Mitochondria volume data of C6 glia cells treated with DOX. (a) The region of interest of digitally stained mitochondria, starting at $t = 0$ min. Zoomed regions I, II, and III are shown. (b) Mitochondria volume changes from initial to final time, $**p = 0.0053$.
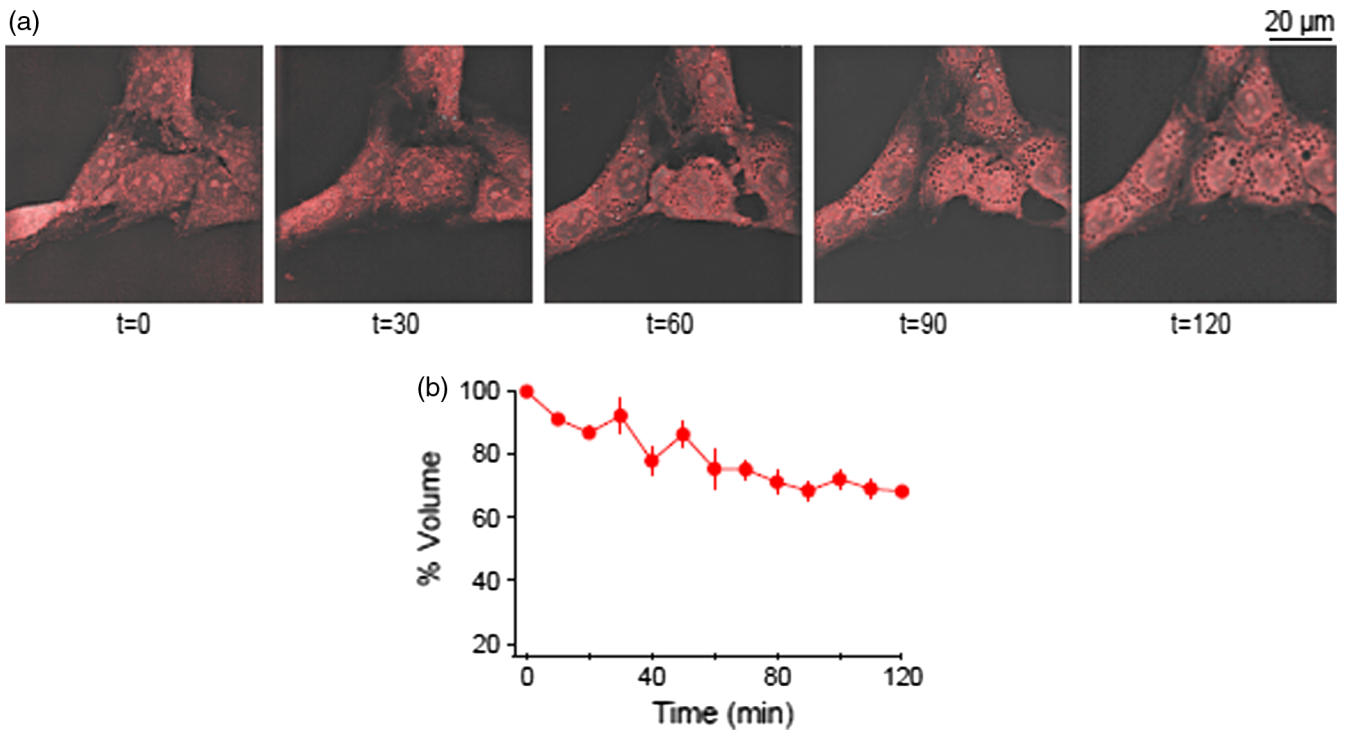

Fig. 4 Cell volume data of C6 glia cells treated with METH. (a) Images of cells after digital staining at $t = 0$ min in 30-min intervals. (b) Apoptotic volume changes.

same through the experiments, this peak was used for normalization.

The intensities of phenylalanine-normalized peaks at 1092, 1155, 1340, 1447, and 1655 cm^{-1} for DOX- and METH-induced apoptosis are shown in Figs. 8 and 9, respectively.

In the DOX-induced apoptotic cell culture, the peak at 1155 cm^{-1} (C–C and C–N stretch of proteins) initially increased in intensity. At the last time point ($t = 150$ min), the intensity decreased. In the cell culture treated with METH, however, the intensity of this peak decreased from the start. The peaks at
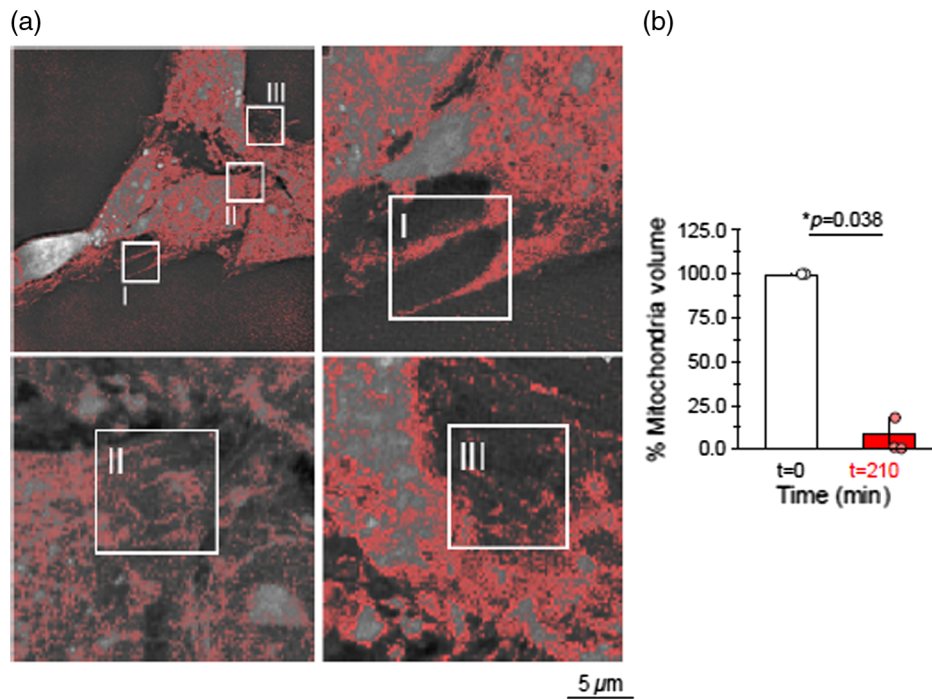
(a)   (b)

5 μm

Fig. 5 Mitochondria volume data of C6 glia cells treated with METH. (a) The region of interest of digitally stained mitochondria, starting at $t = 0$ min. Zoomed regions I, II, and III are shown. (b) Mitochondria volume changes from initial to final time, $*p = 0.038$.
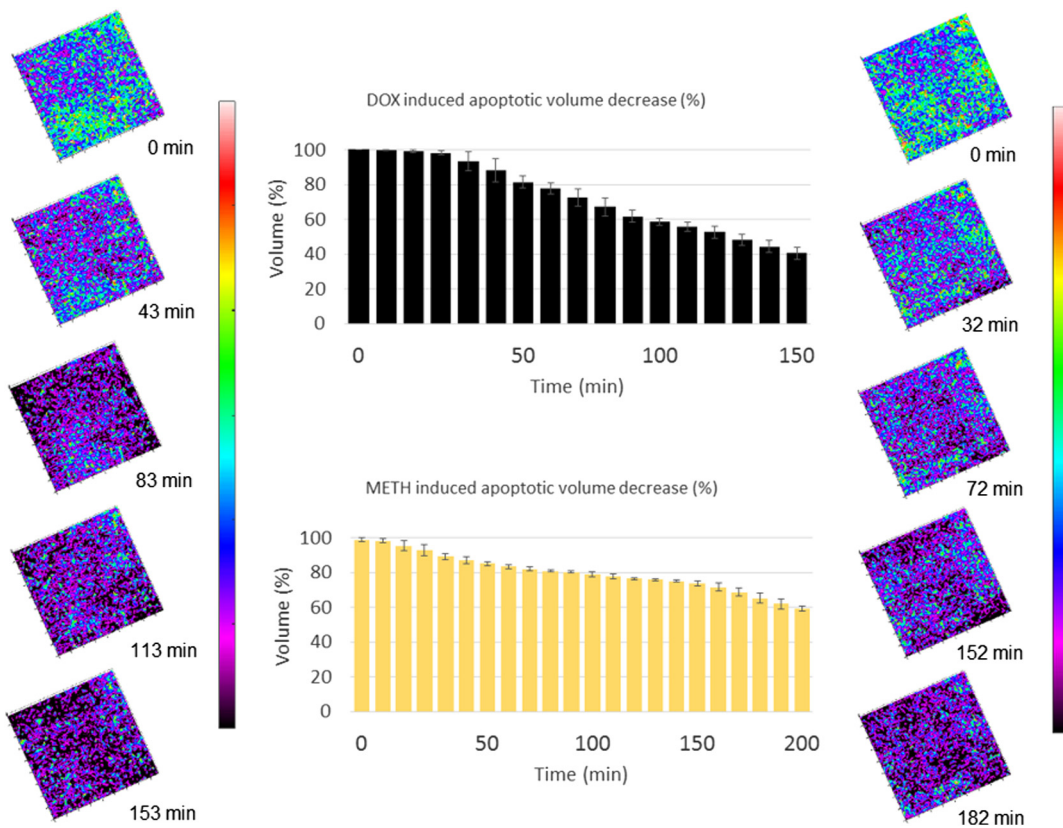

Fig. 6 Apoptotic C6 cell culture volume measurements by DHM. The left panel shows the cell culture treated with DOX (1 μM), and the right panel shows the cell culture treated with METH (100 μM) at various time points after the administering of each drug. The color bar denotes the phase range of 0 to 2π.
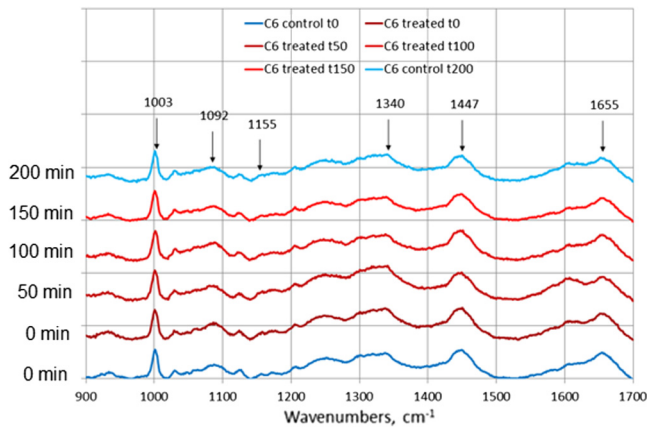
Fig. 7 Raman spectra obtained from cell cultures at various stages of METH-induced apoptosis. Spectra were collected at different time points ($t = 0$ min, $t = 50$ min, $t = 100$ min and $t = 150$ min post METH treatment). Spectra for the untreated controls were taken 200 min apart. The spectra were background subtracted and the peaks were fitted.

1447 cm^{-1} (CH$_2$ bending mode of proteins) and 1661 cm^{-1} (amide I peak) also showed similar behavior (initial increase in intensity followed by a significant drop in DOX, consistent decrease in METH treatment cases). The intensity of DNA (polynucleotide chain) peak at 1340 cm^{-1} has shown initial growth followed by reduction of intensity in both cultures. These results seem to indicate that the breakdown of DNA occurred at an earlier stage in METH-induced apoptosis compared to the DOX-induced one. The behavior of the peak at 1092 cm^{-1} (O–P–O stretch of nucleic acids in DNA) followed a similar pattern: initial growth followed by a reduction in DOX and decreasing intensity in METH.

4 Discussion

In this work, the changes in cell volume and mitochondrial volume of C6 glial cells undergoing apoptosis were monitored by DHM and tomographic phase microscopy, while the chemical changes within these cells were studied by Raman spectroscopy.
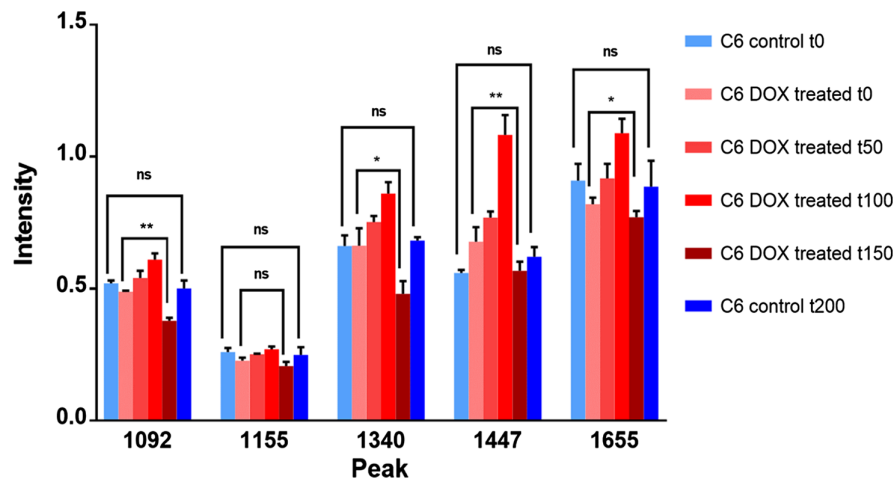
Glial cells exposed to METH exhibited a significant decrease in cell volume, a primary characteristic of apoptosis, which was clearly seen within 40 min post-treatment. Tomographic phase microscopy with the attached environmental chamber allowed accurate measurements of cell volume for a few cells on the nanoscale in real-time.[31]

Our time-course experiments showed that rat C6 glial cell cultures had a cell body loss when treated with either DOX or METH. Recent studies have shown that cellular oxidative stress and mitochondrial dysfunction indicate distinct region-specific cell death signaling events.[62] DOX is a widely used chemotherapeutic agent, which induces apoptosis or cell death via a variety of regulatory mechanisms. The main anticancer action of DOX is believed to involve DNA damage through topoisomerase II inhibition and free-radical generation by a redox reaction. In our study, we used DOX as a positive control. DOX is a known apoptosis inducer, and there are several potential mechanisms of apoptosis induction, so we would anticipate that the cell volume decreases in DOX are higher than those observed with METH. One of the mechanisms of neurotoxicity of METH is the generation of ROS, which then triggers mitochondrial membrane permeability, also called mitochondrial permeability transition (MPT), which is a central co-ordination event in the apoptotic process. MPT causes the release of cytochrome c from mitochondria; cytochrome c then activates effector caspases to induce DNA ladder formation. DOX treatment results in H$_2$O$_2$ generation, leading to the MPT increase, and activates effector caspases to induce apoptosis. Increased drug concentrations may trigger multiple apoptotic mechanisms in the cells. Thus, the observed cell volume change can be attributed primarily to the mechanisms which are triggered and drive the apoptosis process.

Our results for mitochondrial volume showed that a decrease in volume of C6 glial cells started about $t = 50$ min post either DOX (10 μM) or METH (100 μM) treatment, and continued to decrease to minimum detection levels by $t = 120$ min for DOX [Fig. 3(c)] and $t = 160$ min for METH [Fig. 4(c)], respectively. The decrease in mitochondria volume may be attributed to DOX-/METH-induced osmotic swelling and release of lysosomal enzymatic contents into the cytoplasm, triggering a

Fig. 8 Intensities of characteristic Raman peaks for DOX-induced apoptotic and control cell cultures. The phenylalanine peak at 1003 cm^{-1} was used for normalizing peaks at 1092, 1155, 1340, 1447, and 1655 cm^{-1} (peaks: 1092 cm^{-1} **$p = 0.001$, 1340 cm^{-1} **$p = 0.0014$, 1447 cm^{-1} **$p = 0.0067$ and 1655 cm^{-1} *$p = 0.012$; differences are considered significant at $p < 0.05$ (*$p < 0.05$; **$p < 0.01$; ***$p < 0.001$).
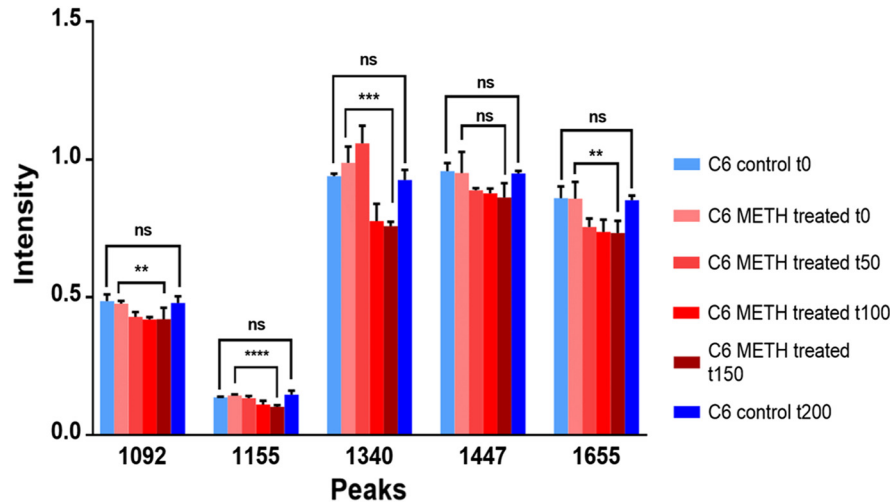
Fig. 9 Intensities of characteristic Raman peaks for METH-induced apoptotic and control cell cultures. The phenylalanine peak at 1003 cm^{-1} was used for normalizing peaks at 1092, 1340, 1447, and 1655 cm^{-1} (peaks: 1092 cm^{-1} *$p = 0.037$, 1155 cm^{-1} ****$p < 0.0001$, 1340 cm^{-1} ***$p = 0.0006$ and 1655 cm^{-1} *$p = 0.012$).

cascade of apoptotic signaling events, which facilitate the relocalization of "cathepsin D" to the cytosol, creating an oxidative environment conducive to a shift toward cell death via activation of mitochondria dependent, caspase-dependent cell signaling events.[63] The mitochondria volume change was not a monotonic decrease but showed fluctuations. This volume at the intermediate time-points also showed higher measurement uncertainties, so it was not clear if these fluctuations were indeed present. The increased uncertainties can be due to the small sample size, or perhaps imperfect digital staining of the cells. This subject requires further study.

Nanolive 3-D Cell Explorer had a 60× air objective, restricting the field-of-view to 85 μm × 85 μm × 0.30 μm. Since large magnification reduced the field-of-view, we were limited in the number of cells that could be observed at a time. This could be one of the reasons for the observed difference in the rate of cell volume decrease between Nanolive and DHM volume measurements for METH-treated samples. It would have required ~50 times more Nanolive image frames to monitor the same number of cells as DHM. The absolute value of the index of refraction ($n = 1.33$) reported by Nanolive measurements was slightly lower than expected and what was reported previously.[37] The difference is, however, within the uncertainty of the index of refraction measurements of the microscope.

Digital staining allowed us to monitor the changes in the volume of glia and observe a significant decrease for both DOX- and METH-treated cultures, separately from the overall volume decrease of the cells. It is worth noting, too, that the overall volume decrease is likely not just due to apoptosis. In the DHM measurements, some of the cells may instead undergo necrosis and/or separate from the substrate, and therefore, their volume will not be counted in the overall volume measurements at the subsequent time points.

An advantage of Nanolive system is that it allowed the monitoring of both the indices of refraction and the cell volume, while DHM generally measures optical thickness, and therefore cannot provide the index of refraction and physical thickness of the sample at the same time. We have, therefore, used the values of the index of refraction obtained from Nanolive measurements in our DHM measurements of cell volume.

DHM with the attached environmental chamber permitted accurate measurements of cell volume for several hundred cells simultaneously, in real time, over the course of the experiment. DHM was used to quantify the effect of METH on cell volume in real time. Our results showed that there was a 40% reduction in cell volume after 150 min, demonstrating that METH induced death in glia cells. We also used Nanolive 3-D Cell Explorer to quantify the effects of METH on cell and mitochondria volumes in real time. By measuring the cell volume of a small number of cells, we produced more detailed nanoscale images.

The same environmental chamber that we deployed with DHM could not, unfortunately, be used for Raman measurements, because the material of the chamber (plastic) was strongly fluorescent under the laser excitation wavelength, making the detection of Raman signal impossible. Therefore, multiple cell samples had to be prepared and removed from an incubator one at a time at each time point to collect its Raman spectrum. Once the sample was out of the incubator, the data had to be collected immediately. The removal of fluorescent background from the petri dish presented another challenge since many of the Raman peaks we were monitoring were partially overlapping with other peaks (see Fig. 6).

Also, it is worth noting that there were some differences in the intensities of Raman peaks between different cell culture dishes, such as the difference between the same peak intensities for control cells in Figs. 8 and 9. In order to be able to do the experiment at the various time points, these cell samples were grown separately, which likely resulted in the sample–sample variation in their Raman spectra.

In the DOX-induced apoptotic cell culture, the peak at 1155 cm^{-1} (C–C and C–N stretch of proteins) initially increased in intensity, presumably because of the accumulation of proteins and progression of nuclear condensation.[64] At the last time point, $t = 150$ min, when the cells were dying, the intensity decreased, which likely pointed to the breakdown of proteins. In the cell culture treated with METH, however, the intensity of this peak began decreasing soon after $t = 0$ min. This may mean that in METH-induced apoptosis, the breakdown of proteins begins earlier.

Our Raman data indicated that the chemical changes in proteins preceded morphological changes detected by the DHM. Despite the fact that volume changes in DOX-induced apoptosis occurred earlier than in METH, we have observed that protein and DNA degradation occurred at the earlier stages in METH-induced apoptosis. This implied that in addition to apoptosis, METH induced other biochemical changes in CNS cells. Of future interest is to evaluate the effects of a range of METH concentrations, in order to determine if there is a certain threshold value of the METH concentration at which cells progress from controlled cell death (apoptosis) to uncontrolled necrosis.

5 Conclusion

We used Nanolive 3-D Cell Explorer and DHM imaging techniques for noninvasive, real-time monitoring of morphological changes in live cells during apoptosis. Both modalities allowed simultaneous visualization of multiple cells. DHM offered several advantages over Nanolive 3-D Cell Explorer, such as its ability to image larger groups of cells (a few hundred) at a time and very fast data acquisition. Meanwhile, Raman spectroscopy was employed to detect chemical changes the cells undergo during apoptosis.

In the future, we plan to collect Raman data differently: the cells will be continuously monitored in the custom-built environmental chamber, similar to the one used in DHM and Nanolive experiments, but free from fluorescent materials. We will be able to follow the same culture for the entire duration of the experiment and monitor Raman peak changes in real time.

Based on the results of this study, it is clear that apoptosis is a well-orchestrated process, which consists of an organized series of events, including both chemical and morphological cell changes, that results in programmed cell death. This study also emphasized that Nanolive 3-D Cell Explorer, DHM, and Raman spectroscopy are imaging tools that can be utilized for noninvasive, real-time, simultaneous monitoring of morphological and chemical changes in cells during apoptosis and could also be applied to monitoring of other dynamic cell processes. Our study provided detailed, time-resolved information about METH-induced damage to brain cells that can be utilized in the search for METH addiction treatment options.

Disclosure

The authors have no relevant financial interests in this article and no potential conflicts of interest to disclose.

Acknowledgments

References

1. X. Deng et al., "Methamphetamine induces apoptosis in an immortalized rat striatal cell line by activating the mitochondrial cell death pathway," *Neuropharmacology* **42**(6), 837–845 (2002).
2. S. Radfar and R. A. Rawson, "Current research on methamphetamine: epidemiology, medical and psychiatric effects, treatment, and harm reduction efforts," *Addict. Health* **6**(3–4), 146–154 (2014).
3. J. P. Zhu, W. Xu, and J. A. Angulo, "Methamphetamine-induced cell death: selective vulnerability in neuronal subpopulations of the striatum in mice," *Neuroscience* **140**(2), 607–622 (2006).
4. C. Davidson et al., "Methamphetamine neurotoxicity: necrotic and apoptotic mechanisms and relevance to human abuse treatment," *Brain Res. Rev.* **36**(1), 1–22 (2001).
5. M. C. Wenlock et al., "A method for measuring the lipophilicity of compounds in mixtures of 10," *J. Biomol. Screen* **16**(3), 348–355 (2011).
6. O. Bergman and D. Ben-Shachar, "Mitochondrial oxidative phosphorylation system (OXPHOS) deficits in schizophrenia: possible interactions with cellular processes," *Can. J. Psychiatry* **61**(8), 457–469 (2016).
7. M. D. Brand and D. G. Nicholls, "Assessing mitochondrial dysfunction in cells," *Biochem. J.* **435**(2), 297–312 (2011).
8. I. K. Tulloch et al., "Methamphetamine induces striatal cell death followed by the generation of new cells and a second round of cell death in mice," *Curr. Neuropharmacol.* **9**(1), 79–83 (2011)
9. X. Deng and J. L. Cadet, "Methamphetamine-induced apoptosis is attenuated in the striata of copper-zinc superoxide dismutase transgenic mice," *Mol. Brain Res.* **83**(1–2), 121–124 (2000).
10. H. S. Sharma and E. A. Kiyatkin, "Rapid morphological brain abnormalities during acute methamphetamine intoxication in the rat. An experimental study using light and electron microscopy," *J. Chem. Neuroanat.* **37**(1), 18–32 (2009).
11. L. R. Martinez et al., "Methamphetamine enhances histoplasmosis by immunosuppression of the host," *J. Infect. Dis.* **200**(1), 131–141 (2009).
12. S. A. Salamanca et al., "Impact of methamphetamine on infection and immunity," *Front. Neurosci.* **8**, 445 (2015).
13. J. L. Cadet et al., "Neurotoxicity of substituted amphetamines: molecular and cellular mechanisms," *Neurotoxic. Res.* **11**(3–4), 183–202 (2007).
14. E. Maeno et al., "Normotonic cell shrinkage because of disordered volume regulation is an early prerequisite to apoptosis," *Proc. Natl. Acad. Sci. U. S. A.* **97**(17), 9487–9492 (2000).
15. Y. Sekine et al., "Methamphetamine causes microglial activation in the brains of human abusers" *J. Neurosci.* **28**(22), 5756–5761 (2008).
16. J. L. Cadet, S. Jayanthi, and X. Deng, "Speed kills: cellular and molecular bases of methamphetamine-induced nerve terminals degeneration and neuronal apoptosis," *FASEB J.* **17**(13), 1775–1788 (2003).
17. J. L. Cadet, S. Jayanthi, and X. Deng, "Methamphetamine—induced neuronal apoptosis involves the activation of multiple death pathways. Review," *Neurotoxic. Res.* **8**(3–4), 199–206 (2005).
18. S. Ares-Santos et al., "Methamphetamine causes degeneration of dopamine cell bodies and terminals of the nigrostriatal pathway evidenced by silver staining," *Neuropsychopharmacology* **39**(5), 1066–1080 (2014).
19. S. Bellini et al., "Neuronal glutamate transporters control dopaminergic signaling and compulsive behaviors," *J. Neurosci.* **38**(4), 937–961 (2018).
20. I. Tsutsui-Kimura et al., "Dysfunction of ventrolateral striatal dopamine receptor type 2-expressing medium spiny neurons impairs instrumental motivation," *Nat. Commun.* **8**, 14304 (2017).
21. S. P. Yu and D. W. Choi, "Ions, cell volume, and apoptosis," *Proc. Natl. Acad. Sci. U. S. A.* **97**(17), 9360–9362 (2000).
22. A. Sharikova et al., "Methamphetamine induces apoptosis of microglia via the intrinsic mitochondrial-dependent pathway," *J. Neuroimmune Pharmacol.* **13**(3), 396–411 (2018).
23. S. Elmore, "Apoptosis: a review of programmed cell death," *Toxicol. Pathol.* **35**(4), 495–516 (2007).
24. R. Parekh and G. A. Ascoli, "Neuronal morphology goes digital, a research hub for cellular and system neuroscience," *Neuron* **77**(6), 1017–1038 (2013).
25. G. Griffths and J. M. Lucoq, "Antibodies for immunolabeling by light and electron microscopy: not for the faint hearted," *Histochem. Cell Biol.* **142**(4), 347–360 (2014).
26. B. Swietek et al., "Immunostaining of biocytin-filled and processed sections for neurochemical markers," *J. Visualized Exp.* **118**, e54880 (2016).
27. R. Alford et al., "Toxicity of organic fluorophores used in molecular imaging: literature review," *Mol. Imaging* **8** (6), 341–354 (2009).
28. R. Kasprowicz, R. Suman, and P. O'Toole, "Characterising live cell behaviour: traditional label-free quantitative phase imaging approaches," *Int. J. Biochem. Cell Biol.* **84**, 89–95 (2017).
29. V. Magidson and A. Khodjakov, "Circumventing photodamage in live-cell microscopy," *Methods Cell Biol.* **114**, 545–560 (2013).
30. S. Filali et al., "Live-stream characterization of cadmium-induced cell death during visible CdTe-QDs," *Sci. Rep.* **8**, 12614 (2018).
31. L. Pollaro, B. D. Piazza, and Y. Cotte, "Digital staining: microscopy of live cells without invasive chemicals," *Microsc. Today* **23**(4), 12–17 (2015).
32. Y. Cotte et al., "Marker-free phase nanoscopy," *Nat. Photonics* **7**(5), 418–418 (2013).

33. A. Ali et al., "Quantitative live single-cell mass spectrometry with spatial evaluation by three-dimensional holographic and tomographic laser microscopy," *Anal. Sci.* **32**, 125–127 (2016).

34. A. Khmaladze, M. K. Kim, and C.-M. Lo "Phase imaging of cells by simultaneous dual-wavelength reflection digital holography," *Opt. Express* **16**, 10900–10911 (2008).

35. J. Kühn et al., "Label-free cytotoxicity screening assay by digital holographic microscopy," *Assay Drug Dev. Technol.* **11**(2), 101–107 (2013).

36. N. Pavillon et al., "Early cell death detection with digital holographic microscopy," *PLoS One* **7**(1), e30912 (2012).

37. A. Khmaladze et al., "Dual-wavelength digital holographic imaging with phase background subtraction," *Opt. Eng.* **51**(5), 055801 (2012).

38. B. Rappaz et al., "Digital holographic microscopy: a quantitative label-free microscopy technique for phenotypic screening," *Comb. Chem. High Throughput Screen.* **17**(1), 80–88 (2014).

39. J. Zheng, P. Gao, and X. Shao, "Opposite-view digital holographic microscopy with autofocusing capability," *Sci. Rep.* **7**(1), 4255 (2017).

40. D. Boss et al., "Measurement of absolute cell volume, osmotic membrane water permeability, and refractive index of transmembrane water and solute flux by digital holographic microscopy," *J. Biomed. Opt.* **18**(3), 036007 (2013).

41. C. Xie, M. A. Dinno, and Y.-Q. Li, "Near-infrared Raman spectroscopy of single optically trapped biological cells," *Opt. Lett.* **27**, 249–251 (2002).

42. M. K. Kim, "Principles and techniques of digital holographic microscopy," *SPIE Rev.* **1**, 018005 (2010).

43. K. Alm et al., "Cells and holograms—holograms and digital holographic microscopy as a tool to study the morphology of living cells," in *Holography—Basic Principles and Contemporary Applications*, E. Mihaylova, Ed., pp. 335–351, InTech, Rijeka (2013).

44. P. Marquet et al., "Digital holographic microscopy: a noninvasive contrast imaging technique allowing quantitative visualization of living cells with subwavelength axial accuracy," *Opt. Lett.* **30**(5), 468–470 (2005).

45. C. V. Raman and K. S. Krishnan, "A new type of secondary radiation," *Nature* **121**, 501–502 (1928).

46. R. Smith, K. Wright, and L. Ashton, "Raman spectroscopy, an evolving technique for live cell studies," *Analyst* **141**, 3590–3600 (2016).

47. M. Wahadoszamen et al., "Laser Raman spectroscopy with different excitation sources and extension to surface enhanced Raman spectroscopy," *J. Spectrosc.* **2015**, 1–8 (2015).

48. P. I. Okagbare et al., "Noninvasive Raman spectroscopy of rat tibiae: approach to *in vivo* assessment of bone quality," *J. Biomed. Opt.* **17**(9), 090502 (2012).

49. A. Khmaladze et al., "Human oral mucosa tissue-engineered constructs monitored by Raman fiber-optic probe," *Tissue Eng. C* **21**, 46–51 (2015).

50. W. Lo et al., "Raman spectroscopy monitoring of the cellular activities of a tissue-engineered ex vivo produced oral mucosal equivalent," *J. Raman Spectrosc.* **42**, 174–178 (2011).

51. A. Khmaladze et al., "Tissue-engineered constructs of human oral mucosa examined by Raman spectroscopy," *Tissue Eng. C* **19**(4), 299–306 (2013).

52. J. D. McElderry, M. R. Kole, and M. D. Morris, "Repeated freeze-thawing of bone tissue affects Raman bone quality measurements," *J. Biomed. Opt.* **16**(7), 071407 (2011).

53. M. Schulmerich et al., "Noninvasive Raman tomographic imaging of canine bone tissue," *J. Biomed. Opt.* **13**(2), 020506 (2008).

54. K. A. Dooley et al. "Stress mapping of undamaged, strained, and failed regions of bone using Raman spectroscopy," *J. Biomed. Opt.* **14**(4), 044018 (2009).

55. Q. Matthews et al., "Variability in Raman spectra of single human tumor cells cultured in vitro: correlation with cell cycle and culture confluency," *Appl. Spectrosc.* **64**, 871–887 (2010).

56. H. Sadeghi-Alibadi et al., "Cytotoxic evaluation of doxorubicin in combination with simvastatin against human cancer cells," *Res. Pharm. Sci.* **5**(2), 127–133 (2010).

57. S. Aydinlik et al., "Enhanced cytotoxic activity of doxorubicin through the inhibition of autophagy in triple negative breast cancer cell line," *Biochim. Biophys. Acta* **1861**, 49–57 (2017).

58. V. Sandoval et al., "Methamphetamine-induced rapid and reversible changes in dopamine transporter function: an in vitro model," *J. Neurosci.* **21**(4), 1413–1419 (2001).

59. L. Basova et al., "Dopamine and its receptors play a role in the modulation of CCR5 expression in innate immune cells following exposure to methamphetamine: implications to HIV infection," *PLoS One* **13**(6), e0199861 (2018).

60. H. Yao et al., "Raman spectroscopic analysis of apoptosis of single human gastric cancer cells," *Vibrat. Spectrosc.* **50**, 193–197 (2009).

61. A. Sharikova et al., "Monitoring of live cell cultures during apoptosis by phase imaging and Raman spectroscopy," *Proc. SPIE* **10074**, 100740V (2017).

62. D. Y. Lee et al., "Distinct pools of non-glycolytic substrates differentiate brain regions and prime region-specific responses of mitochondria," *PLoS One* **8**(7), e68831 (2013).

63. R. Yamaguchi and G. Perkins, "Dynamics of mitochondrial structure during apoptosis and the enigma of Opa1," *Biochim. Biophys. Acta* **1787**(8), 963–972 (2009).

64. A. Zoladek et al., "Non-invasive time-course imaging of apoptotic cells by confocal Raman micro-spectroscopy," *J. Raman Spectrosc.* **42**, 251–258 (2011).

Lianna Y. D'Brant received her master's in physics at the State University of Albany while researching under Dr. Alexander Khmaladze and Dr. Annalisa Scimemi. Under Dr. Khmaladze, she studied the cellular morphological changes of cultured C6 rat glial cells induced by methamphetamine using different imaging modalities. She is currently working at the Neural Stem Cell Institute pursuing her interest in neuroscience, developing therapeutic intercellular antibodies for degenerative diseases associated with misfolding proteins, such as Alzheimer's, Parkinson's, and Huntington's disease.

Habben Desta is a research volunteer in the University at Albany, SUNY Physics Department and an undergraduate pursuing a bachelor's degree in Nanoscale Engineering at the SUNY Polytechnic Institute Colleges of Nanoscale Science and Engineering. Her research interests pertain the mechanobiology of cancer and metastasis. She is currently in her senior year of undergraduate study and plans on beginning her PhD in chemical and biomolecular engineering at Johns Hopkins University in the fall.

Ting Chean Khoo is a second year PhD student in the Physics Department at the University at Albany (SUNY), New York. His research interests include Raman hyperspectral imaging and digital holographic microscopy of nonbiological and biological samples.

Anna V. Sharikova has research interests in developing and use of laser-based spectroscopic and imaging systems, such as Raman spectroscopy and digital holographic microscopy, for characterization of various biological samples, as well as programming for scientific applications.

Supriya D. Mahajan is an associate professor in the Department of Medicine, Jacobs School of Medicine & Biomedical Sciences, University at Buffalo, New York. Her research work is focused on effects of drug abuse on blood-brain barrier (BBB) integrity and function as it pertains to neuroinflammation, drug delivery, and nanotherapeutics. She has validated 2-D and 3-D *in-vitro* human BBB models that allow evaluation of drug premeability and mechanisms that underlie BBB modulation and pathophysiology.

Alexander Khmaladze has gradually expanded his work into the domains of chemistry and biology, having been trained as a physicist. He specializes in microscopic imaging and spectroscopy. His research interests include Raman spectroscopy and microscopy, three-dimensional digital holographic imaging, scanning microscope design, hyperspectral imaging of live cells, and biological tissue imaging.